JACS
JOURNAL OF THE AMERICAN CHEMICAL SOCIETY
ARTICLE
pubs.acs.org/JACS

Ca_3N_2 and Mg_3N_2: Unpredicted High-Pressure Behavior of Binary Nitrides

Cordula Braun,[†] Saskia L. Börger,[†] Teak D. Boyko,[‡] Gerhard Miehe,[§] Helmut Ehrenberg,[§,⊥] Peter Höhn,[¶] Alexander Moewes,[‡] and Wolfgang Schnick[†,*]

[†]Ludwig-Maximilians-Universität München, Department Chemie, Butenandtstrasse 5-13, D-81377 München, Germany

[‡]Department of Physics and Engineering Physics, University of Saskatchewan, 116 Science Place, Saskatoon, Saskatchewan, S7N 5E2 Canada

[§]Institut für Materialwissenschaft, Technische Universität Darmstadt, Petersenstr. 23, D-64287 Darmstadt, Germany

[⊥]Karlsruhe Institute of Technology (KIT), Institute for Applied Materials (IAM), Hermann-von-Helmholtz-Platz 1, D-76344 Eggenstein-Leopoldshafen, Germany

[¶]Max-Planck-Institut für Chemische Physik fester Stoffe, Nöthnitzer Str. 40, D-01187 Dresden, Germany

ABSTRACT: High-pressure synthesis allows both fundamental and materials science research to gain unprecedented insight into the inner nature of materials properties at extreme environment conditions. Here, we report on the high-pressure synthesis and characterization of γ-Ca_3N_2 and the high-pressure behavior of Mg_3N_2. Investigation of M_3N_2 (M = Ca, Mg) at high-pressure has been quite challenging due to the high reactivity of these compounds. Ex situ experiments have been performed using a multianvil press at pressures from 8 to 18 GPa (1000−1200 °C). Additional in situ experiments from 0 to 6 GPa (at RT) at the multianvil press MAX 80 (HASYLAB, Beamline F.2.1, Hamburg) have been carried out. The new cubic high-pressure phase γ-Ca_3N_2 with anti-Th_3P_4 defect structure exhibits a significant increase in coordination numbers compared to α-Ca_3N_2. Contrary, Mg_3N_2 shows decomposition starting at surprisingly low pressures, thereby acting as a precursor for Mg nanoparticle formation with bcc structure. Soft X-ray spectroscopy in conjunction with first principles DFT calculations have been used to explore the electronic structure and show that γ-Ca_3N_2 is a semiconductor with inherent nitrogen vacancies.

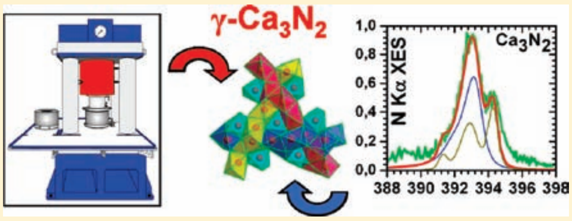

■ INTRODUCTION

High-pressure synthesis is the method of choice to access the still vast realm of superhard materials and promising new phases, being widely used and highly sought after for various applications. The first compelling high-pressure synthesis of diamond in 1953[1] initiated the quest for novel synthetic superhard materials.[2] Subsequent synthesis of c-BN[3] is widely regarded as the milestone of artificial superhard material synthesis and has stimulated the growing interest in this field of research. Nowadays, there is a notable interest in high-pressure research targeting novel extreme condition phases of elements[4,5] or compounds featuring new and exciting properties (e.g., high-temperature superconductivity).[6−8]

The behavior of binary nitrides under extreme conditions has been an important research field triggered by the discovery of γ-Si_3N_4.[9] Such nitridic spinels exhibit a remarkable increase in coordination numbers (CN), resulting in significantly increased hardness and materials properties suitable for industrial applications. High-pressure phases of chemically and thermally stable nitrides have recently been investigated thoroughly owing to their various applications and exciting properties. Nitrides M_3N_4 (M = Hf, Zr)[10] were found to have Th_3P_4 structure with high CN ($M^{[8]}$) and advanced properties (e.g., high hardness).[10] The (anti-)Th_3P_4 structure, which has been found for the new high-pressure phase as well, exhibits a broad range of characteristics[11,12] and provides promising candidates for superconducting behavior.[13,14] The experimental results[10] have been confirmed by DFT calculations[15] and illustrate the potential still dormant in the multifaceted family of nitride materials. The high-pressure (HP)-behavior of binary nitrides is diverse and less predictable than expected, even α-C_3N_4, a carbon(IV)nitride with complete sp^3 hybridization of the C atoms, is still elusive[16] and only theoretically predicted, whereas a novel binary tantalum nitride[17] with U_2S_3 structure has become recently accessible by high-pressure synthesis.

α-Ca_3N_2 (antibixbyite-type) has various industrial applications, which include precursors for host lattices of rare-earth doped phosphors in LEDs,[18] catalysts for the crystallization of c-BN[19,20] or as gas-generating agent in airbags.[21] Furthermore, the Ca_3N_2−CaNH-system has been studied as a promising candidate for hydrogen storage.[22] The yellow high temperature (HT) phase of Ca_3N_2,[23] previously thought to be γ-Ca_3N_2, has recently been identified as calcium dinitride cyanamide $Ca_4[CN_2]N_2$[24] and a potential high-pressure/high-temperature (HP/HT) phase[25] has not been explored further.

Received: July 21, 2010
Published: March 09, 2011

Recently described β-Ca_3N_2[26] (anti-Al_2O_3-structure) as well as various applications of α-Ca_3N_2 (e.g., as starting material for the synthesis of binary alkaline earth nitrides) underline the interest in this compound. Novel high-pressure modifications of Ca_3N_2 are not only interesting from a scientific point of view but also relevant based on their potential hydrogen storage capabilities for example in the system Ca_3N_2—CaNH,[22] which may lead to further applications.

Theoretical calculations have been reported by Römer et al.,[27,28] which predict the existence of several hitherto unknown HP-phases of Ca_3N_2 and Mg_3N_2. The selected models base on the HP-behavior of corundum. Concerning the high-pressure behavior of M_3N_2 (M = Ca, Mg), there are experimental and theoretical investigations of Hao et al.,[29,30] of which the theoretical results are in agreement with the ones of Römer et al.[27,28] However, the proposed high-pressure phases are not supported by the experimental XRD patterns displayed in refs 29 and 30. The appearance of two new weak reflections is most probable due to reactions of M_3N_2 (M = Ca, Mg) with the used but inappropriate pressure medium silicone oil.

These comprehensive studies have led to intensive investigations of the HP-behavior of the binary nitrides M_3N_2 (M = Ca, Mg).

EXPERIMENTAL SECTION

Synthesis. For the investigations of the high-pressure behavior of Ca_3N_2 and Mg_3N_2 the starting materials α- and β-Ca_3N_2 and α-Mg_3N_2 (99.5%, Aldrich Chemical Co., Milwaukee) were used. The quality of α-/β-Ca_3N_2 and α-Mg_3N_2 was ascertained by powder X-ray diffraction and elemental analysis; no impurities (esp. C, H, O) were detected. For a detailed description of the synthesis of α- and β-Ca_3N_2 see ref 26.

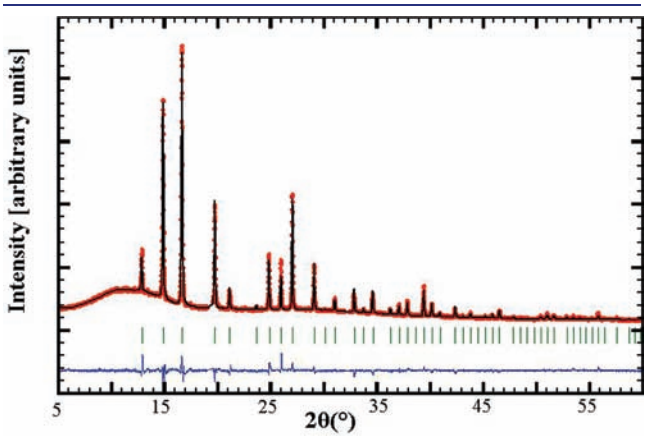

Figure 1. γ-Ca_3N_2: Observed (circles) and calculated (line) X-ray powder diffraction pattern together with their difference curve after Rietveld refinement (λ = 0.709026 Å).

High-Pressure Synthesis of γ-Ca_3N_2 and bcc—Mg. The high-pressure syntheses of γ-Ca_3N_2 and bcc—Mg were carried out using the multianvil technique[31−33] with a hydraulic press. All sample preparation had to be done in argon atmosphere and to prevent the sample from oxidation during the experiment it was additionally surrounded by an inert and protecting metal foil. Ex situ experiments with the multianvil press have been conducted at the following pressures and temperatures: 8, 12 GPa at ∼1000 °C and 14, 16, 18 GPa at ∼1200 °C. Cr_2O_3-doped MgO octahedra (Ceramic Substrates & Components Ltd., Isle of Wight) with edge lengths of 14 and 10 mm were used for pressures up to 12 and 18 GPa, respectively.

Exemplarily only one pressure and temperature program will be described in the following. Eight truncated tungsten carbide cubes separated by pyrophyllite gaskets served as anvils for the compression of the octahedra. The truncation edge length for the 14/8 assembly was 8 mm. Powder of ambient-pressure M_3N_2 (M = Ca, Mg) was loaded into a cylindrical capsule of hexagonal boron nitride (Henze, Kempten) with a capacity of 9 mm^3 (14/8 assembly) and sealed with a BN cap. The capsule was centered within two nested graphite tubes, which acted as an electrical resistance furnace. The remaining volume at both ends of the sample capsule was filled out with two cylindrical pieces of magnesium oxide. The arrangement was placed into a zirconium dioxide tube and then transferred into a pierced MgO octahedron. The electrical contact of the graphite tubes was arranged by two plates of molybdenum. For the 8 GPa experiment the assembly was compressed at room temperature within 2.5 h and then heated up to 1000 °C within 12 min. Under these conditions, the sample was treated for 12 min and cooled down to 600 °C within 30 min. After that the sample was quenched to room temperature, followed by a decompression of 7.5 h. Using high-pressure synthesis, γ-Ca_3N_2 and Mg_3N_2 (including bcc—Mg) were obtained as red and yellow-grayish substances, respectively. The temperature was calculated from the electrical power applied to the furnace, which was determined on the basis of calibration curves from measurements with a thermocouple, which is directly connected to an Eurotherm 2404 temperature controller (Limburg a. d. Lahn, Germany). Therefore, some uncertainties in the specific synthesis temperatures result but are within a sufficiently narrow temperature range not to affect the observed phase formation. For temperatures up to 1500 °C Pt—$Pt_{87}Rh_{13}$ was used as a thermocouple, above 1500 °C W_3Re_{97}—$W_{25}Re_{75}$ (SPPL—010, SP13RH—010, W3W25—010, Newport Omega, Deckenpfronn, Germany). For the pressure calibration as a function of hydraulic oil pressure, the commonly used phase transitions in Bi (the I—II at 2.55 GPa, II—III at 3.15 GPa and III—V transition at 7.70 GPa) and the semiconductor to metal transitions

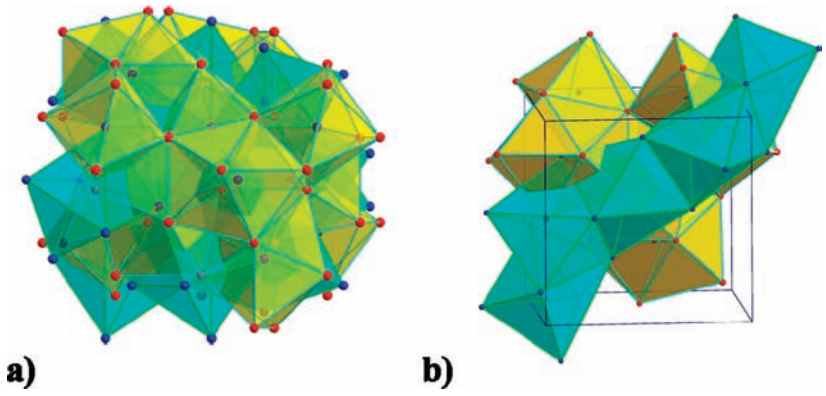

Figure 2. a) and b) corner, edge and face sharing octahedra (turquoise) and dodecahedra (yellow) forming the anti-Th_3P_4 structure type.

Table 1. Crystallographic Data of γ-Ca_3N_2 Derived from Rietveld Refinement

formula	γ-Ca_3N_2
formula mass/g mol^{-1}	148.26
crystal system	cubic
space group	$I\bar{4}3d$ (no. 220)
cell parameters/Å	$a = 7.7212(3)$
cell volume/Å^3	460.32(3)
formula units/cell	5 1/3
diffractometer	STOE STADI P
radiation/Å	Mo−Kα_1 ($\lambda = 0.70926$ Å)
monochromator	Ge (111)
temperature/K	293
data range (2θ), step width	$5° \leq 2\theta \leq 60°$, 0.01°
structure refinement	Rietveld refinement, *Fullprof*[36]
background treatment	15 fixed background points
profile function	pseudo-Voigt (no. 7)
R_{Bragg}	7.89
GOF	2.1
reduced χ^2	4.55

in ZnTe (15.5 GPa) and GaAs (18.3 GPa) have been performed. A detailed description of temperature and pressure calibration can be found in refs 31 and 34 and the references therein.

In situ High-Pressure Measurements. In situ high-pressure measurements for Ca_3N_2 and Mg_3N_2 (0 to 6 GPa at RT) were performed with the multianvil high-pressure apparatus MAX80 (NRD Tsukuba, Japan), which is located at the Hamburger Synchrotronstrahlungslabor (HASYLAB, Beamline F.2.1) for in situ high-pressure and high-temperature X-ray diffraction investigations. Energy-dispersive diffraction patterns are recorded using white X-rays from the storage ring DORIS III. The pressure was measured by using the high-pressure equation of state for admixed NaCl by Decker.[35] The beamline is equipped with a Ge solid-state detector, situated at the press frame and tracking the adjustment of the whole apparatus in relation to the X-ray beam. The multianvil apparatus is equipped with six tungsten carbide anvils, which are driven by a 2.500 N uniaxial hydraulic ram. The top and bottom anvil are driven directly, the lateral anvils by two load frames and four reaction bolsters. The maximum pressure for the 8 mm cube setup is approximately 9 GPa with temperatures up to 1600 °C, which are produced by an internal graphite heater. The high-pressure cell consists of a cube made of boron epoxy resin and the gaskets between the anvils are formed from the boron epoxy cube's material during the runs. The high-pressure cell (BN) is filled with the ground sample, the graphite heater, the pressure standard (NaCl) and the thermocouple, which is insulated by boron nitride. All sample preparation was done in argon atmosphere and the sample was protected by an additional metal foil. Rings made from heated pyrophyllite provide electrical insulation and act as a quasi-hydrostatic pressure transmitting medium. Copper rings contact the heater at the top and bottom anvils.

Powder X-ray Diffraction. The obtained crystallites were too small for single-crystal X-ray diffraction analysis, so the structure refinements of γ-Ca_3N_2 and bcc−Mg were based on ex situ X-ray powder diffraction data. X-ray diffraction experiments on the products of the high-pressure reactions of Ca_3N_2 and Mg_3N_2 were performed on a STOE STADI P powder diffractometer in Debye−Scherrer geometry with Ge(111)-monochromatized Mo-Kα_1 radiation ($\lambda = 0.709026$ Å). The samples were enclosed in glass capillaries with 0.5 mm diameter. A Rietveld refinement was carried out using the program package *Fullprof*.[36]

Details of the X-ray data collection, structural refinements, final equivalent atomic coordinates and isotropic displacement parameters are listed in Tables 1−7. Further details of the crystal structure investigations can be obtained from the Fachinformationszentrum Karlsruhe, 76344 Eggenstein-Leopoldshafen, Germany (fax: (+49)7247−808−666, e-mail: crysdata@fiz-karlsruhe.de) on quoting the depository numbers CSD-421950 and CSD-421951.

EDX Measurements. The samples were also analyzed by energy-dispersive X-ray micro analysis where only the elements Ca and Mg as well as N were detected in the γ-Ca_3N_2 and Mg_3N_2 phases, respectively. A carbon coated sample was examined with a scanning electron microscope (SEM) JSM-6500F (Joel, Japan, maximum acceleration voltage 30 kV). Qualitative and semiquantitative elemental analyses were carried out using an energy dispersive spectrometer (Model 7418, Oxford Instruments, United Kingdom).

Soft X-ray Spectroscopy and DFT Calculations. The X-ray emission spectroscopy (XES) measurements was performed at the Advanced Light Source (Berkley, CA, USA) on beamline 8.0.1,[37] whereas X-ray absorption spectroscopy (XAS) measurements (measured in total fluorescence yield mode) took place at the Canadian Light Source (Saskatoon) on the SGM beamline.[38] The samples were prepared by pressing small fragments of calcium nitride into freshly scraped indium foil under argon atmosphere (the samples were never exposed to an oxygen or nitrogen environment). The N Kα XES and N 1s XAS were calibrated in energy using *h*-BN with the peaks near were the band gap located at 394.4 and 402.1 eV, respectively. The calculations were performed using the *WIEN2k* density functional theory (DFT) software[39] utilizing the generalized gradient approximation of Perdew−Burke−Ernzerhof (GGA−PBE).[40] A (9, 9, 3) k-point mesh integration with − 6.0 Ryd plane wave cutoff was used. The RMT spheres for both the nitrogen and calcium atoms were 2.26 Bohr with an RK_{max} of 7.0. The XAS spectra were simulated with a full core hole potential correction. For further details on simulating XAS and XES with *WIEN2k*, see ref 41.

■ RESULTS AND DISCUSSION

In this work, we have investigated the HP/HT-behavior of the binary nitrides Ca_3N_2 and Mg_3N_2 employing the multianvil technique. The new dark red high-pressure phase γ-Ca_3N_2 was ex situ obtained by applying pressures between 8 and 18 GPa and temperatures below 1200 °C starting from ambient pressure α-Ca_3N_2, as well as β-Ca_3N_2.[26] In situ investigations at the synchrotron showed the phase transformation already at much lower pressures (0.8 GPa). HP/HT-investigations of Mg_3N_2 were carried out in a multianvil press at pressures from 8 to 18 GPa (1000−1200 °C) and in situ from 0 to 6 GPa (at RT), starting from ambient pressure α-Mg_3N_2. All handling had to be done in argon atmosphere as Ca_3N_2 and Mg_3N_2 are extremely air sensitive. Furthermore, the high-pressure experiments and the ex situ investigations also required special oxygen and moisture free conditions.

Structural Analysis of γ-Ca_3N_2. The powder pattern of γ-Ca_3N_2 (Figure 1) matched a cubic body-centered lattice with lattice parameter $a = 7.7212(3)$ Å. All observed systematic extinctions correspond only to one space group, namely $I\bar{4}3d$ (no. 220). The crystal structure of the nitrides M_3N_4 (M = Zr, Hf),[10] crystallizing in the same space group, provided the starting model for the structure solution. Table 1 shows crystallographic data and details of the Rietveld refinement of γ-Ca_3N_2 and Table 2 displays the occupied Wyckoff sites, refined atomic coordinates and isotropic displacement parameters. Estimated standard deviations are calculated in agreement with ref 42.

Structure Description of γ-Ca_3N_2. The new high-pressure phase γ-Ca_3N_2 is the first binary nitride derived from the multi-faceted anti-Th_3P_4 structure type family which exhibits a broad

Table 2. Occupied Wyckoff Sites, Refined Atomic Coordinates and Isotropic Displacement Parameters B_{iso} (in Å^2) of γ-Ca_3N_2 (Standard Deviation in Parentheses)

atom	Wyck.	*x*	*y*	*z*	s.o.f.	B_{iso}
Ca	16*c*	0.04762(7)	0.04762(7)	0.04762(7)	1	1.86(3)
N	12*a*	3/8	0	1/4	0.88[a]	2.61(2)

[a] calculated value from composition; refined occupancy for N: 0.93(3).

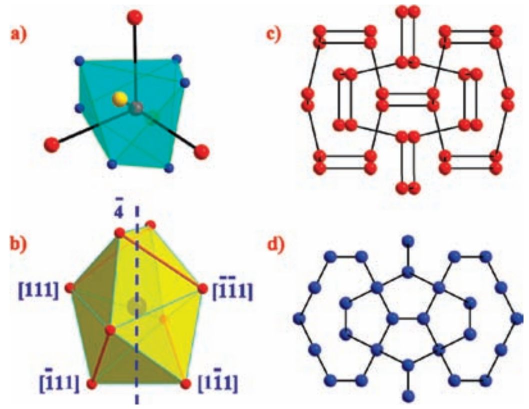

Figure 3. **a)** Ca^{2+}-octahedron with five next Ca-atoms (distances: Ca (red)−Ca (red) = 3.21 Å, Ca (red)−Ca (yellow) = 3.34 Å), **b)** N^{3-}-dodecahedron (yellow) with the $\bar{4}$ and the four different ⟨111⟩ directions in a rod packing, the 3-fold axes (orange) run along the edges of the dodecahedron, **c)** Ca^{2+}-lattice forming a 10,3-net, **d)** N^{3-}-lattice, (Ca (red) N (blue)).

spectrum of compositions (e.g., A_3B_4 with A = La, Ce, Pr, Nd, Tb, Dy, Ho, B = Ge, Sb, Bi[43] or Rb_4O_6[44] and Pu_2C_3).[45] γ-Ca_3N_2 ($[Ca^{2+}]_4([N^{3-}]_{2.67}[\square]_{0.33})$ constitutes a disordered defect variant of the anti-Th_3P_4 type (Figure 2). Vacancy and charge ordering phenomena of this structure type have been discussed in detail elsewhere.[46] The significant increase in CN from α-Ca_3N_2 to γ-Ca_3N_2, facilitated by high-pressure synthesis, is in accordance with the pressure-coordination rule.[47] α-Ca_3N_2 has CN = 4 for Ca^{2+}, forming tetrahedra with N^{3-} ligands. The Ca^{2+}-ions in γ-Ca_3N_2 are topologically 6-fold coordinated (part a of Figure 3), and the effective number of neighbors is 5.33 due to the defect structure. Face sharing of the octahedra is realized by the five next Ca-atoms. For N^{3-} the CN increases from 6 in α-Ca_3N_2 to 8 in γ-Ca_3N_2, building distorted dodecahedra. The distances within the polyhedra can be divided into two groups: one with short distances and one with long ones (Table 3). The Ca^{2+}-octahedra as well as the N^{3-}-dodecahedra (Figure 2) are condensed through common faces and are additionally interlinked through corners and edges. Subsequently, octahedral and dodecahedral polyhedra form columns running along the body diagonals ⟨111⟩ of the cubic unit cell.

O'Keeffe et al.[48] proposed a new approach to further characterize the complex crystal structure of the (anti-)Th_3P_4 structure type family. The authors introduced rod packings (Figure 4) or columns as a unifying principle to simplify the characterization of intricate crystal structures. They used a bcc rod packing scheme, as depicted in part a of Figure 4, to describe the Th_3P_4 structure with the nearest neighbors of a given atom along the ⟨111⟩ directions, and all of the atoms of the structure are located on rods along these directions.

Bärnighausen et al.[11] however described the Th_3P_4 structure by analyzing the enantiomeric 10,3-networks with cubic symmetry formed by the anion lattice (e.g., Sm_3S_4)[11] opposed to the rod packings description used by O'Keeffe and co-workers.[48] The 10,3-networks form two chiral networks whose structure depends upon their respective angles (part c of Figure 3).

Table 3. Selected Bond Lengths (in Angstroms) and Angles (in Degrees) of γ-Ca_3N_2, (Standard Deviations in Parentheses)

atom	distance
Ca−N (3*x*)	2.4027(5)
Ca−N (3*x*)	2.9944(5)
N−Ca (4*x*)	2.4027(5)
N−Ca (4*x*)	2.9944(5)
Ca−Ca (3*x*)	3.2106(8)
Ca−Ca (2*x*)	3.3434(8)
Ca−Ca (2 + 4*x*)	3.5014(8)
N−N	3.6113(1)

atom	angle
N−Ca−N (3*x*) short dist.	97.442(18)
N−Ca−N (3*x*) long dist.	74.170(15)
Ca−N−Ca (2*x*) short dist.	93.55(3)
Ca−N−Ca (2*x*) short dist.	151.20(4)
Ca−N−Ca (2*x*) long dist.	64.84(2)
Ca−N−Ca (2*x*) long dist.	135.45(3)

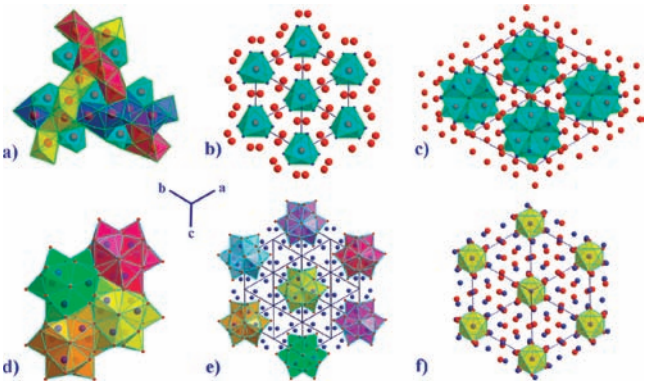

Figure 4. **γ-Ca_3N_2: a)** bcc rod packing of Ca^{2+}-octahedra (yellow, turquoise, pink and green) parallel to different ⟨111⟩, **b)** pattern of rods of Ca^{2+}-octahedra running along ⟨111⟩, **d)** and **e)** rods of N^{3-}-dodecahedra viewed along ⟨111⟩, **α-Ca_3N_2:** rods of c) Ca^{2+}-tetrahedra and f) N^{3-}-octahedra running along ⟨111⟩, (Ca (red) N (blue)).

Comparison of α-, β-, and γ-Ca_3N_2. In α-Ca_3N_2 as well as in γ-Ca_3N_2, both Ca^{2+}- and N^{3-}-ions form rods along ⟨111⟩. The rod packing concept is a powerful tool for the comparison of α-Ca_3N_2 with the HP-phase. The directions ⟨111⟩ in α-Ca_3N_2 are only partially occupied by Ca^{2+}-ions, contrary to γ-Ca_3N_2. The connectivity of the polyhedra only through corners and edges in α-Ca_3N_2 leads to a layered pattern with vacancies due to the missing connection through common faces. The lack of these vacancies in γ-Ca_3N_2 generates an increased density compared to α-Ca_3N_2.

The density increases significantly from α-Ca_3N_2 (2.60 gcm^{-3}) to β-Ca_3N_2 (2.69 gcm^{-3}) and to γ-Ca_3N_2 (2.85 gcm^{-3}), resulting in a difference of 9.6% (Table 4). The γ-Ca_3N_2 phase has a notably higher density (2.85 gcm^{-3}) compared to the

Table 4. Comparison of α-, β-, and γ-Ca_3N_2

Ca_3N_2	S.G.	cell [Å]	Wyck./ Ca	ρ [g cm^{-3}]	V [Å^3]	V/atom [Å^3]
α	$Ia\bar{3}$(no.206)	a = 11.47	48e	2.60	1502	18.87
β	$R\bar{3}c$ (no.167)	a = 6.19 c = 16.62	18e	2.69	550	18.43
γ	$I\bar{4}3d$ (no.220)	a = 7.72	16c	2.85	460	17.25

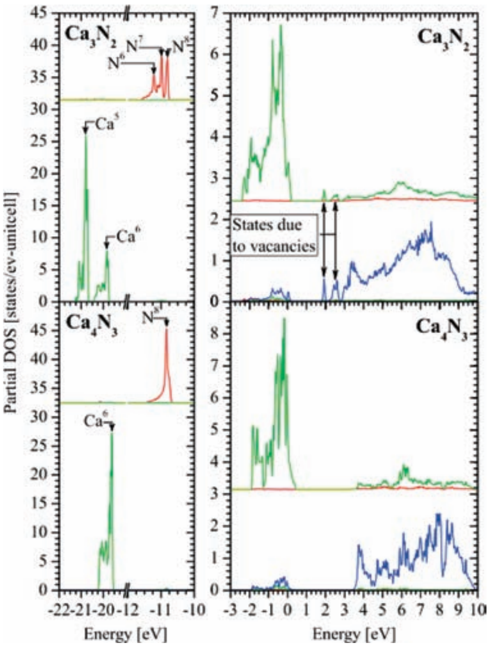

Figure 5. Calculated partial density of states (pDOS) for the nitrogen sites are displayed in the top portion of each panel, calcium in the lower portion. The s-states (red), p-states (green), and d-states (blue) are color-coded. The pDOS are offset vertically by an arbitrary value for display purposes; the relative pDOS value remains accurate. The introduction of nitrogen vacancies splits the tightly bound states (N s and Ca p) and creates localized states in the band gap. These tightly bound states are labeled N[x] and Ca[y] (where x and y refer to the number of N nearest neighbors).

calculated value of 2.79 g·cm^{-3} by Römer et al.[27] for the theoretically predicted γ-phase (anti-Rh_2O_3—II structure) expected to form between 5 and 10 GPa. According to the principle of Le Chatelier this precludes the existence of the above calculated phase as our experiments established the in situ formation of cubic γ-Ca_3N_2 beginning at 0.8 GPa.

The structure types of the three hitherto identified Ca_3N_2 modifications show no direct group—subgroup symmetry relations. The phase transitions from the metastable β-Ca_3N_2 with anticorundum structure to α-Ca_3N_2 as well as γ-Ca_3N_2 are reconstructive. α-Ca_3N_2 and γ-Ca_3N_2 can be described by the rod-packing concept employing different types of rods, but this model cannot be applied to the β-phase because its structure is distinctly characterized by layers. β-Ca_3N_2 is probably a low-temperature phase, which is metastable at room temperature and based on its observation at 5 K has a higher density compared to the α-phase (there is a β to α transition at 810 K).[26] Therefore, the formation of γ-Ca_3N_2 from α-Ca_3N_2 might proceed via an intermediate formation of β-Ca_3N_2.

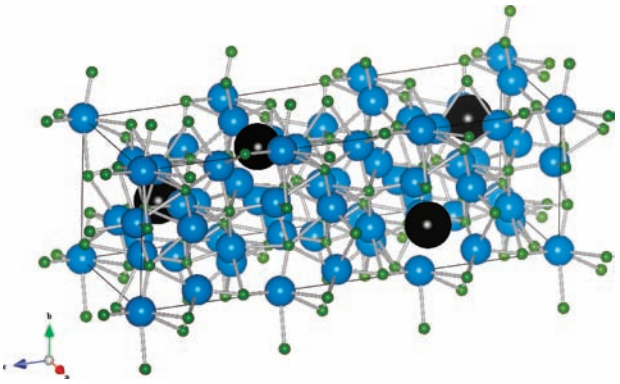

Figure 6. Super cell used to calculate the DOS of Ca_3N_2. The calcium, nitrogen, and vacancies are displayed in blue, green, and black, respectively.

Soft X-ray Spectroscopy and DFT Calculations of γ-Ca_3N_2. Soft X-ray spectroscopy in conjunction with first principles DFT calculations can elucidate the chemical bonding and electronic behavior of γ-Ca_3N_2 and gain additional insight into its structure. Two different superstructure models — one with and one without nitrogen vacancies — are compared. The partial densities of states (pDOS) calculated using DFT are shown in Figure 5, where the vacancy model (referred to hereafter as Ca_3N_2), is compared to the nonvacancy model (referred to hereafter as Ca_4N_3). If we assume that all atoms would prefer to exist in their formal oxidation states, Ca^{2+} and N^{3-}, then the molecular formula should be Ca_3N_2 requiring that 1.333 ($1 + {}^{1}/_{3}$) N atoms must be removed from the unit cell. This is achieved with a 1 × 1 × 3 supercell in which four nitrogen atoms are removed. The vacancies are uniformly distributed in such a way that there is no bond ordering and thus results a space group symmetry that is now $P1$ (all crystallographic sites are nonequivalent, Figure 6).

The DOS for both models (Figure 5) suggests that bonding in this material is strongly ionic in the sense that most of the Ca valence electrons have been transferred to the N atoms. The evidence for this is manifested in that the valence band (which is energetically localized and about 2 eV wide) is predominately comprised of occupied N p-states. The conduction band, however, consists predominately of unoccupied Ca d-states. The valence and conduction band contribution of the Ca- and N-states respectively are negligible. Such ionic bonding character further supports the vacancy model because N vacancies are necessary for all atoms to exist in their formal oxidation states. The effect of the N vacancies is readily seen in the pDOS in both the low-energy conduction band states and the sub-valence band (sub-band) states. The tightly bonded sub-bands (Ca 3p and N 2s) are split into the contributions of the Ca and N nonequivalent sites and occur due to the creation of nonequivalent sites in Ca_3N_2. There are eight Ca atoms surrounding all three N sites, however the next coordination shell including the missing N atoms (vacancies) perturbs the electronic structure creating multiple localized states (Figure 7). This is further illustrated by the Ca p-band splitting between the Ca atoms with and without an N atom missing from their octahedron. In the conduction band, the nitrogen vacancies create interband states, which play a key role in distinguishing the model that best simulates the experimental measurements because this seems to be the only observable difference in the electronic states.

The pDOS of this material suggests that it possesses some very interesting electronic properties. In particular for Ca_4N_3, there is a substantial amount of valence electron states that are unfilled

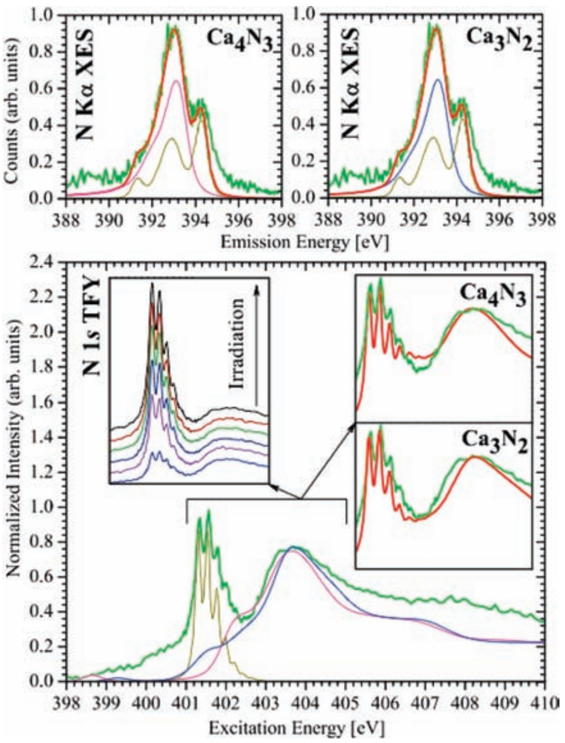

Figure 7. Experimental X-ray emission spectra (XES) and X-ray absorption spectra (measured in total fluorescence mode − TFY). The experimental spectra are shown in green, the simulated spectra (appropriately broadened with a pseudo-Voigt function) are shown in blue (Ca_3N_2) and magenta (Ca_4N_3). The reference N_2 spectra from refs 49 (XES) and 50 (TFY) shown in brown are added to the calculated spectra, which takes into account the N_2 gas in the material. In successive scans the amount of trapped N_2 increases. The comparison of the added spectra (red) with the measured spectra (green) favors the inclusion of N vacancies.

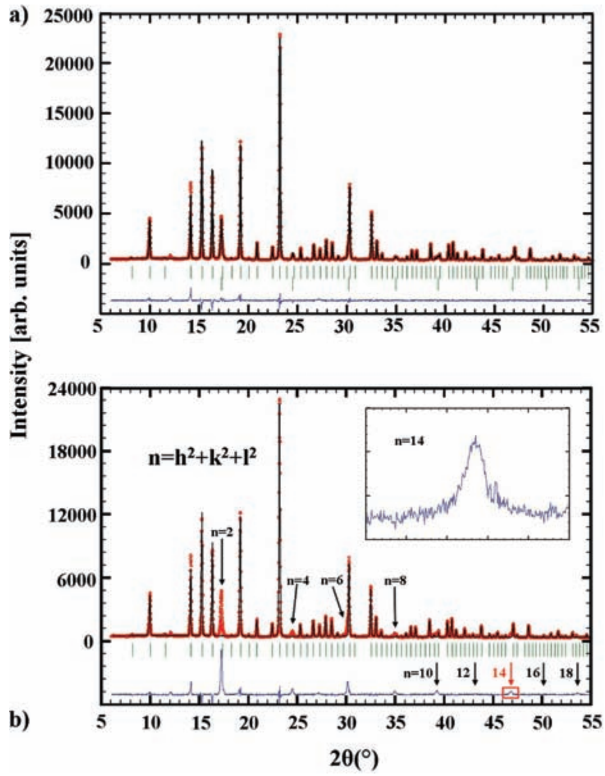

Figure 8. a) Observed (circles) and calculated (line) X-ray powder diffraction pattern together with their difference curve after Rietveld refinement (λ = 0.709026 Å). The upper row of reflection marks corresponds to Mg_3N_2 and the lower one to HP−Mg (10% w/w), b) X-ray powder diffraction pattern of only Mg_3N_2. The reflections in the difference plot correspond to HP−Mg.

suggesting that this material exhibits semimetal properties. These unfilled valence states are diminished when the structure includes N vacancies; the unfilled states in Ca_4N_3 and Ca_3N_2 are 0.768*e* and 0.519*e*, respectively. These materials have a calculated direct band gap of 2.59 and 1.64 eV for Ca_4N_3 and Ca_3N_2, respectively. Strictly speaking this is not the energy separation between occupied and unoccupied states but a forbidden energy gap within the unoccupied states. The band gap of Ca_3N_2 shrinks due the decrease in periodic symmetry of the Ca and N sites within the lattice creating interband states at the bottom of the conduction band. Therefore, the N vacancies increase the semiconductor nature of calcium nitride. Calcium nitride has a tendency to hydrolyze readily, therefore only the nitrogen spectral measurements are presented since the calcium measurements are distorted due to inherent CaO surface contamination. These experimental measurements compared to those simulated using DFT calculations of Ca_4N_3 and Ca_3N_2 are shown in Figure 7. The measurements themselves create interstitial N_2 (gas) within the material as a result of X-ray irradiation. Taking successive XAS scans and noting that the N_2 portion of spectra increases in intensity with progressive exposure to radiation is a verification of this. There is clear evidence that an N_2 gas contribution exists in both the XES and XAS spectra (Figure 7), therefore calculated N_2 spectra[49,50] have been added to the simulated calcium nitride spectra to account for this contribution and provide a more meaningful comparison between measured and simulated spectra. The N Kα XES spectra do not allow us to determine whether N vacancies are present due to the large lifetime broadening the spectra exhibit − both models agree equally well with the experimental measurements. The N 1s XAS spectra show a larger sensitivity to N vacancies; the vacancies reduce the band gap and produce states further away from the large feature at ~404 eV (previously mentioned in the DOS). In the region from 401 to 404 eV, the experimental spectrum is best reproduced by the Ca_3N_2 simulation, confirming that there are N vacancies present in the material. The feature at 398.8 and 399.2 eV (Figure 7) for Ca_4N_3 and Ca_3N_2 respectively is diminished for Ca_3N_2. Because this feature is not present in the measured spectrum this would suggest that vacancies must be present (the presence of the core hole reduces the intensity of this feature from that seen in the DOS). Whereas both simulated spectra of Ca_4N_3 and Ca_3N_2 have a quite satisfactory fit, the Ca_3N_2 model fits significantly better.

High-Pressure Behavior of Mg_3N_2. *Structural Analysis of bcc−Mg.* Concerning the high-pressure behavior of Mg_3N_2, ex situ multianvil experiments at 9 GPa showed no changes in the powder diffraction pattern of α-Mg_3N_2, apart from further crystallization. However at 12 GPa new reflections appeared in the powder pattern (part a of Figure 8). The newly formed phase remains metastable after quenching for several hours at room temperature and ambient pressure. At first, the structure determination for the new phase was attempted corresponding to the structure solution of γ-Ca_3N_2. The refined structure did not match with the measured pattern, which precluded a HP−Mg_3N_2 phase with anti-Th_3P_4 structure. Furthermore, the structure did not belong to any of the predicted phases for Mg_3N_2 calculated by Römer, Hao, and co-workers.[28,29] The new reflections could be indexed based on a body-centered cubic (bcc) unit cell with $a = 3.3381(2)$ Å and $V = 37.19$ Å^3. Without additional extinction rules and based on reasonable interatomic distances within the small unit cell volume, the structure of bcc metals with $Im\bar{3}m$ (no. 229) space group symmetry (Table 5) and only atoms on the 2a-site (0, 0, 0) is proposed (Table 6). Estimated standard deviations are calculated in agreement with ref 42.

For illustration of the contribution from the bcc−Mg phase to the powder diffraction pattern, a simulated pattern of only α-Mg_3N_2 was compared with the measured pattern. The difference plot marks the peaks of bcc−Mg very clearly (part b of Figure 8). Note that an alternative indexing, based on a primitive cubic (pc) structure with $a_{pc} = a_{bcc}/\sqrt{2}$ is not possible. The reflection with $n_{bcc} = h^2 + k^2 + l^2 = 14$ is observed and cannot be explained by the alternative pc structure, because $n_{pc} = 7$ is not possible. Such diffraction patterns have been observed under in situ conditions as well, where only Mg can form such a bcc−metal structure. Rietveld refinement[36] confirmed the formation of about 10% (w/w) bcc−Mg with a volume-weighted averaged crystallite diameter between 30 and 35 nm.

High-Pressure Behavior of Mg. In high-pressure studies Olijnyk et al.[52] observed the formation of bcc−Mg from hcp−Mg at 58 GPa and the transition back to the hcp phase during pressure release at 44 GPa. The bcc modification found by Olijnyk et al.[52] at 58 GPa (and measured at that pressure) has a compressed lattice parameter ($a = 2.9539$ Å) and a considerably decreased volume ($V = 25.77$ Å^3) compared to our values, which

Table 5. Crystallographic Data of HP−Mg Derived from Rietveld Refinement

formula	Mg
formula mass/g mol^{-1}	24.30
crystal system	cubic
space group	$Im\bar{3}m$ (no. 229)
cell parameters/Å	$a = 3.3381(2)$
cell volume/Å^3	37.1963(9)
formula units/cell	2
diffractometer	STOE STADI P
radiation/Å	Mo−Kα_1 ($\lambda = 0.70926$ Å)
monochromator	Ge 111 (curved)
temperature/K	293
data range (2θ), step width	$5° \leq 2\theta \leq 56°$, 0.01°
structure refinement	Rietveld refinement, *Fullprof*[36]
background treatment	17 fixed background points
profile function	pseudo-Voigt (no. 7)
R_{Bragg}	2.84
GOF	1.7
reduced χ^2	3.05

Table 6. Occupied Wyckoff Sites, Refined Atomic Coordinates, and Isotropic Displacement Parameters B_{iso} (in Å^2) of Mg (hcp)[51] and HP−Mg (bcc), (Standard Deviation in Parentheses)

	atom	Wyck.	x	y	z	s.o.f.	B_{iso}
Mg (hcp)	Mg	2*c*	1/3	2/3	1/4	1	0.49(5)
HP−Mg (bcc)	Mg	2*a*	0	0	0	1	0.44(14)

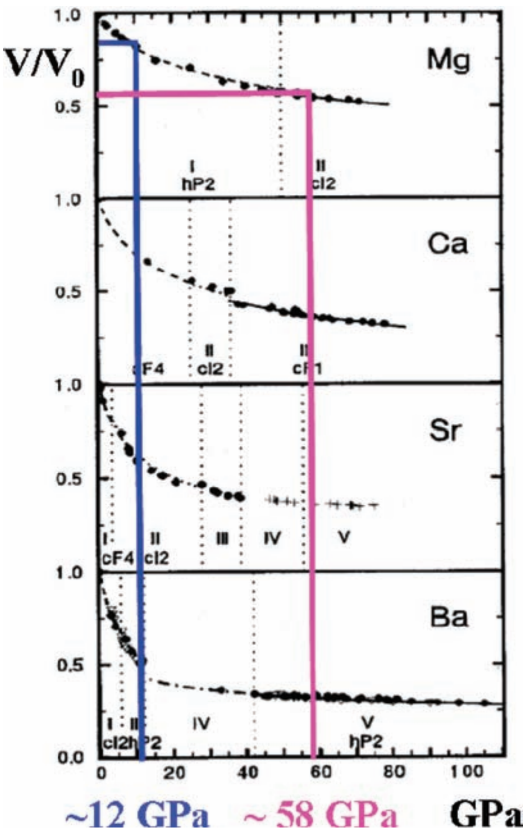

Figure 9. Equation of State of Mg:[51−53] V/V_0-data of HP−Mg ($V/V_0 = 0.80$) at 12 and 58 GPa[53] ($V/V_0 = 0.55$).

Table 7. Comparison of Mg (hcp) and HP−Mg (bcc),

	Mg (hcp)	HP−Mg (bcc)	
crystal system	hexagonal[51]	cubic	cubic[52,53]
space group	$P\,6_3/mmc$ (no. 194)	$Im\bar{3}m$ (no. 229)	$Im\bar{3}m$ (no. 229)
cell parameters/Å	$a = 3.20$ $c = 5.21$	$a = 3.33$	$a = 2.95$ (at 586Pa)
cell volume/Å^3	46.48	37.19	25.75
formula units/cell	2	2	
density/ρ	1.73	2.17	3.14
formation pressure	ambient pressure	2 (in situ)/ 12 (ex situ) GPa	58−48 (in situ) GPa
distance Mg−Mg/Å	3.19 (12*x*)	2.89 (8*x*)	2.55 (8*x*)

is due to the extremely high pressure. A rough estimate of the bulk modulus B using these[52] and our data coincide perfectly with the EOS measurements of Mg up to 70 GPa made by Winzenick et al.[53] (Figure 9) in a reasonable order of magnitude (mean $B \approx$ 160 GPa).

These HP-phase transitions are well-known for metals (e.g., Cs,[54] Yb,[55,56] Y).[57] Note that the required pressure for the formation of HP-phases can significantly be reduced for nanosized particles, even down to ambient conditions.[58] The pressure-induced elimination of nitrogen from Mg_3N_2 causes the formation of nanosized[58] Mg-particles because of diffusion-limited crystallite growth. Mg_3N_2 is therefore a suitable precursor for the preparation of a metastable high-pressure bcc−Mg phase at very moderate pressures (e.g., ex situ 12 GPa and in situ 2 GPa) working via precipitation of nanosized Mg metal during decomposition. For a comparison of Mg (hcp) and HP−Mg (bcc), see Table 7. The formation of the high-pressure bcc phase instead of the hcp phase of Mg can be explained with surface curvature effects[58] of the nanoparticles as well as *d*-electron effects resulting from the lowering and partial filling of the initially unoccupied 3d-band with sufficiently high pressure.[59] The tendency of Mg_3N_2 to decompose under extreme conditions might constitute a fine precursor for industrial applications, but at the same time renders any predicted high-pressure phase of Mg_3N_2 improbable.

CONCLUSIONS

In this work, we investigated the high-pressure behavior of the alkaline earth binary nitrides Ca_3N_2 and Mg_3N_2. These two compounds present an entirely different behavior, which might be due to the fact that calcium is much larger and therefore much more compressible than magnesium. With the larger Ca the high-pressure structure seems to be stabilized, whereas no phase transformation takes place for Mg_3N_2 but the smaller magnesium is only forced out of the structure.

Ca_3N_2 forms the very dense high-pressure phase γ-Ca_3N_2 at 9 GPa, with a new defect structure type for binary nitrides. The intricate anti-Th_3P_4 structure type exhibits high CN (for $Ca^{[6]}$ (topologically) and $N^{[8]}$) and has already shown interesting materials properties in numerous compounds. The ab initio DFT calculations suggest that $([Ca^{2+}]_4([N^{3-}]_{2.67}[\square]_{0.33})$ may even have semimetal properties, but to a lower degree compared with a hypothetical Ca_4N_3, which was also taken into consideration. The calcium nitrogen bonding is highly ionic and shows a large amount of charge transfer suggesting that the N and Ca exist in their formal oxidation states. The simulated γ-Ca_3N_2 spectra (for a vacancy model) reproduce the measured calcium nitride spectra best. To conclude, the high-pressure calcium nitride structure has a propensity to form N vacancies. In contrast to the high-pressure behavior of Ca_3N_2, Mg_3N_2 shows decomposition behavior starting already at moderate pressures (at room temperature). The advancing bcc modification of elemental Mg nanoparticles is metastably quenchable and might be a promising precursor for the customized design of new compounds with promising properties and new applications.

AUTHOR INFORMATION

Corresponding Author

wolfgang.schnick@uni-muenchen.de

ACKNOWLEDGMENT

The authors gratefully acknowledge financial support from the Fonds der Chemischen Industrie and the Deutsche Forschungsgemeinschaft (priority program SPP 1236, project SCHN 377/13) Germany. We further would like to thank the Natural Sciences and Engineering Research Council of Canada (NSERC) and the Canada Research Chair Program. Tom Z. Regier from the Canadian Light Source (CLS) is acknowledged for his help in setting up the measurements at CLS.

REFERENCES

(1) Bundy, F. P.; Hall, H. T.; Strong, H. M.; Wentorf, R. H. *Nature* **1955**, *176*, 51.

(2) McMillan, P. F. *Nat. Mater.* **2002**, *1*, 19.

(3) Wentorf, R. H. *J. Chem. Phys.* **1957**, *26*, 956.

(4) Oganov, A. R.; Chen, J.; Gatti, C.; Ma, Y.; Ma, Y.; Glass, C. W.; Liu, Z.; Yu, T.; Kurakevych, O. O.; Solozhenko, V. L. *Nature* **2009**, *457*, 863.

(5) Zarechnaya, E. Yu.; et al. *Phys. Rev. Lett.* **2009**, *102*, 185501–1.

(6) Amaya, K.; Shimizu, K.; Eremets, M. I. *Int. J. Mod. Phys. B* **1999**, *13*, 3623.

(7) Eremets, M. I.; Gregoryanz, E. A.; Struzhkin, V. V.; Mao, H.-K.; Hemley, R. J.; Mulders, N.; Zimmerman, N. M. *Phys. Rev. Lett.* **2000**, *83*, 2797.

(8) Eremets, M. I.; Struzhkin, V. V.; Mao, H.-K.; Hemley, R. J. *Science* **2001**, *293*, 272.

(9) Zerr, A.; Miehe, G.; Serghiou, G.; Schwarz, M.; Kroke, E.; Riedel, R.; Fuess, H.; Kroll, P.; Boehler, R. *Nature* **1999**, *400*, 340.

(10) Zerr, A.; Miehe, G.; Riedel, R. *Nat. Mater.* **2003**, *2*, 185.

(11) Heim, H.; Bärnighausen, H. *Acta Crystallogr., Sect. B* **1978**, *34*, 2084.

(12) Flahaut, J.; Guitard, M.; Patrie, M.; Pardo, M.; Golbai, S.; Domange, L. *Acta Crystallogr.* **1965**, *19*, 14.

(13) Wang, X.; Loa, I.; Syassen, K.; Kremer, R.; Simon, A.; Hanfland, M.; Ahn, K. *Phys. Rev. B* **2005**, *72*, 064520–1.

(14) Westerhold, K.; Timmer, F.; Bach *Phys. Rev. B* **1985**, *32*, 2985.

(15) Kroll, P. *Phys. Rev. Lett.* **2003**, *90*, 125501–1.

(16) Horvath-Bordon, E.; Riedel, R.; Zerr, A.; McMillan, P. F.; Auffermann, G.; Prots, Y.; Bronger, R.; Kniep, R.; Kroll, P. *Chem. Soc. Rev.* **2006**, *35*, 987.

(17) Zerr, A.; Miehe, G.; Li, J.; Dzivenko, D. A.; Bulatov, V. K.; Höfer, H.; Bolfan-Casanova, N.; Fialin, M.; Brey, G.; Watanabe, T.; Yoshimura, M. *Adv. Funct. Mater.* **2009**, *19*, 2282.

(18) Hirosaki, N.; Uheda, K.; Yamamoto, H. PCT WO/2005/052087 A1.

(19) Solozhenko, V. L.; Turkevich, V. Z.; Will, G. *J. Am. Ceram. Soc.* **1996**, *79*, 2798.

(20) Bocquillon, G.; Loriers-Susse, C.; Loriers, J. *J. Mater. Sci.* **1993**, *28*, 3547.

(21) Akihiko, T.; Kaoru, M.; Kenjirok, I.; Ryo, M.; Moriyoshi, K.; Makoto, I.; Akihiko, K.; Eishi, S.; K.Takeshi, Eiichiro, Y.; , EP 0952131 A1.

(22) Xiong, Z.; Chen, P.; Wu, G.; Lin, J.; Tan, K. L. *J. Mater. Chem.* **2003**, *13*, 1676.

(23) Laurent, Y.; David, J.; Lang, J. *C. R. Acad. Sci. Paris* **1964**, *259*, 1132.

(24) Reckeweg, O.; DiSalvo, F. *Z. Anorg. Allg. Chem.* **2001**, *627*, 371.

(25) Bradley, R.; Munro, D.; Whitfield, M. *J. Inorg. Nucl. Chem.* **1966**, *28*, 1803.

(26) Höhn, P.; Hoffmann, S.; Hunger, J.; Leoni, S.; Nitsche, F.; Schnelle, W.; Kniep, R. *Chem.—Eur. J.* **2009**, *15*, 3419.

(27) Römer, S. R.; Schnick, W.; Kroll, P. *J. Phys. Chem. C* **2009**, *113*, 2943.

(28) Römer, S. R.; Dörfler, T.; Kroll, P.; Schnick, W. *Phys. Status Solidi B* **2009**, *246*, 1604.

(29) Hao, J.; Li, Y.; Zhou, Q.; Liu, D.; Li, M.; Li, F.; Lei, W.; Chen, X.; Ma, Y.; Cui, Q.; Zou, G.; Liu, J.; Li, X. *Inorg. Chem.* **2009**, *48*, 9737.

(30) Hao, J.; Li, Y. W.; Wang, J. S.; Ma, C. L.; Huang, L. Y.; Liu, R.; Cui, Q. L.; Zou, G. T.; Liu, J.; Li, X. D. *J. Phys. Chem. C* **2010**, *114*, 16750.

(31) Huppertz, H. *Z. Kristallogr.* **2004**, *219*, 330.

(32) Walker, D.; Carpenter, M. A.; Hitch, C. M. *Am. Mineral.* **1990**, *75*, 1020.

(33) Walker, D. *Am. Mineral.* **1991**, *76*, 1092.

(34) Rubie, D. C. *Phase Trans.* **1999**, *68*, 431.

(35) Decker, D. L. *J. Appl. Phys.* **1971**, *42*, 3239.

(36) Rodriguez-Carvajal, J. *Fullprof.2k* − version 4.40, 2008.

(37) Jia, J. J.; Callcott, T. A.; Yurkas, J.; Ellis, A. W.; Himpsel, F. J.; Samant, M. G.; Stöhr, J.; Ederer, D. L.; Carlisle, J. A.; Hudson, E. A.; Terminello, L. J.; Shuh, D. K.; Perera, R. C. C. *Rev. Sci. Instrum.* **1995**, *66*, 1394.

(38) Regier, T.; Krochak, J.; Sham, T. K.; Hu, Y. F.; Thompson, J.; Blyth, R. I. R. *Nucl. Instrum. Methods Phys. Res., Sect. A* **2007**, *582*, 93.

(39) Schwarz, K.; Blaha, P.; Madsen, G. K. H. *Comput. Phys. Commun.* **2002**, *147*, 71.

(40) Perdew, J. P.; Burke, K.; Ernzerhof, M. *Phys. Rev. Lett.* **1996**, *77*, 3865.

(41) Boyko, T. D.; Bailey, E.; McMillan, P. F.; Moewes, A. *Phys. Rev. B* **2010**, *81*, 155207.

(42) Berar, J. F.; Lelann, P. *J. Appl. Crystallogr.* **1991**, *24*, 1.

(43) Honke, D.; Parthé, E. *Acta Crystallogr.* **1966**, *21*, 435.

(44) Jansen, M.; Korber, N. *Z. Anorg. Allg. Chem.* **1991**, *598/599*, 163.

(45) Zachariasen, W. *Acta Crystallogr.* **1952**, *5*, 17.

(46) Carter, F. *J. Solid State Chem.* **1972**, *5*, 300.

(47) Neuhaus, A. *Chimia* **1964**, *18*, 93.

(48) O'Keeffe, M.; Andersson, S. *Acta Crystallogr., Sect. A* **1977**, *33*, 914.

(49) Glans, P.; Skytt, P.; Gunnelin, K.; Guo, J.-H.; Nordgren, J. *J. Electron Spectrosc. Relat. Phenom.* **1996**, *82*, 193.

(50) Rubensson, J.-E.; Neeb, M.; Biermann, M.; Xu, Z.; Eberhardt, W. *J. Chem. Phys.* **1993**, *99*, 1633.

(51) Straumanis, M. E. *J. Appl. Phys.* **1949**, *20*, 726.

(52) Olijnyk, H.; Holzapfel, W. B. *Phys. Rev. B* **1985**, *31*, 4682.

(53) Winzenick, M.; Holzapfel, W. B. In *High Pressure Science and Technology, Proceedings of the Joint XV AIRAPT and XXXIII EHPRG International Conference on High Pressure Science and Technology*; Trzeciakowski, W. A., Ed.; 384; World Scientific Publ. Co.: Singapore, 1996.

(54) Takemura, K.; Syassen, K. *Phys. Rev. B* **1985**, *32*, 2213.

(55) Takemura, K.; Syassen, K. *J. Phys. F: Met. Phys.* **1985**, *15*, 543.

(56) Kayser, F. X. *Phys. Status Solidi A* **1971**, *8*, 233.

(57) Vohra, Y. K.; Olijnik, H.; Grosshans, W.; Holzapfel, W. B. *Phys. Rev. Lett.* **1981**, *47*, 1065.

(58) Guo, B.; Harvey, A. S.; Neil, J.; Kennedy, I. M.; Navrotsky, A.; Risbud, S. H. *J. Am. Ceram. Soc.* **2007**, *90*, 3683.

(59) Moriarty, J. A.; McMahan, A. K. *Phys. Rev. Lett.* **1982**, *48*, 809.